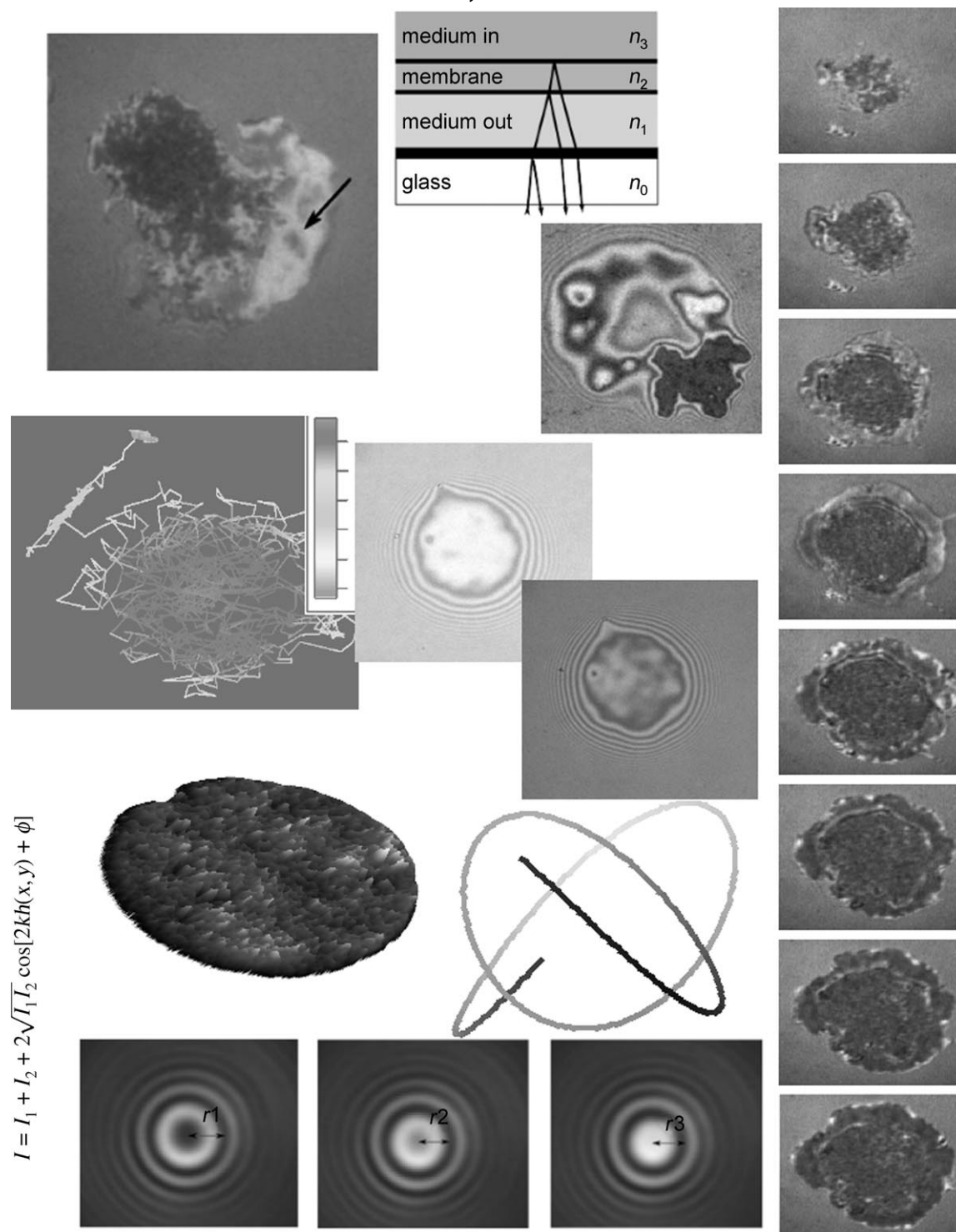


Quantitative Reflection Interference Contrast Microscopy (RICM) in Soft Matter and Cell Adhesion

Laurent Limozin^{*[a]} and Kheya Sengupta^[b]

Dedicated to Erich Sackmann on the occasion of his 75th birthday



Adhesion can be quantified by measuring the distance between the interacting surfaces. Reflection interference contrast microscopy (RICM), with its ability to measure inter-surface distances under water with nanometric precision and milliseconds time resolution, is ideally suited to studying the dynamics of adhesion in soft systems. Recent technical developments, which include innovative image analysis and the use of multi-coloured illumination, have led to renewed interest in this

technique. Unambiguous quantitative measurements have been achieved for colloidal beads and model membranes, thus revealing new insights and applications. Quantification of data from cells shows exciting prospects. Herein, we review the basic principles and recent developments of RICM applied to studies of dynamical adhesion processes in soft matter and cell biology and provide practical hints to potential users.

1. Introduction

To study interactions between surfaces, it is necessary to accurately measure the distance between them. Yet, for certain kinds of surfaces, especially those that are stable or functional only in an aqueous environment, this seemingly simple task remains a challenge. Interference of light is routinely used to measure small inter-surface separations, for example in the famous Michelson–Morley experiments. In fact, application of the technique stretches back to the time of Isaac Newton. In the 1960s, Adam Curtis had the idea of using the same principle to measure the distance between a glass substrate and the underside of a living cell adhering to it, under water, and observed through an optical microscope.^[1] He named this technique “interference reflection microscopy” or IRM. In the years after the first publication, a flurry of activity followed.^[2–5] A great number of improvements and refinements were proposed, but it was soon realized that there was a fundamental limitation to the accuracy of the measurements—the inherent optical inhomogeneity of living cells. All interference-based measurements ultimately rely on a detailed knowledge of the refractive index of the object under study. This meant that as far as living cells were concerned, in the absence of additional information about the complex optical nature of the cell, the distance measurements remained at best qualitative. For this reason, the interest in quantitative IRM slowly died and it was soon used only as a qualitative indicator of adhesion.^[6,7]

In the 1980s Sackmann and co-workers started applying the closely related technique of “reflection interference contrast microscopy” or RICM to surfaces that are much better behaved in terms of their optics^[8,9]—surfaces such as those of colloidal beads, lipid bilayers or membranes of unilamellar vesicles. RICM, with its improved contrast, is perfectly suitable for quantitative measurement of inter-surface distances where one of the surfaces is that of a planar transparent substrate. The image recorded with RICM is a two-dimensional matrix of intensities. With certain mathematical treatment, the intensities are converted to the corresponding substrate/object distance. While the lateral resolution of RICM is set by the limits of conventional optical microscopy, the vertical distance resolution, measured with the help of interference, can go down to 2 nm for optically well defined, static objects. Recently, by taking advantage of modern digital cameras and fast data storage, RICM has been used to probe a variety of dynamical phenomena in-

cluding adhesion of vesicles, the dynamics of colloidal beads close to a surface, single-molecule receptor–ligand kinetics and, admittedly with less precision in the height determination, even cell adhesion. In fact, with the insight gained from working with simpler objects, RICM is now poised to also be adapted for quantitative work with cells.

A few key advances have been made in RICM in the last five years. One crucial advance was the introduction of dual (and later, multi)-wave RICM, which removes the difficulty of identification of the phase associated with any interference technique, and thus enables absolute height measurements.^[10] The next important improvement was the realization that the circular symmetry of the fringes formed by colloidal beads can be exploited to track them robustly with great accuracy—1 nm in the vertical and 10 nm (sub-pixel) in the lateral direction.^[10,11] For vesicles, a new way of analysing the data, based purely on considerations of refractive indices of the reflecting surfaces, which additionally takes into account reflection from multiple interfaces arising from the finite nature of the vesicle membrane, opened the way for very accurate mapping of the topography of the underside of the vesicle.^[12] Integrating the new multi-interface analysis with dual-wave RICM opens up the way for absolute height determination for fluctuating membranes. Another novel analysis technique that has been recently introduced is dynamical RICM, which uses fluctuations as a tool to detect bond clusters that are not detectable otherwise.^[13]

These innovations, along with older experimental and theoretical work, make RICM a very powerful technique to study inter-surface interactions, in particular adhesion. It has the added advantage of not requiring any labelling of the sample, and can be implemented with relative ease and very little investment on a standard inverted microscope. It can also be combined with several other microscopic techniques, such as fluorescence,^[4,14] as well as with force transducers, for example optical or magnetic tweezers.^[13,15,16] In spite of all these advantages, it remains a relatively unknown and underused techni-

[a] Dr. L. Limozin
Adhesion and Inflammation, CNRS UMR 6212, Inserm U600
Aix-Marseille University, Luminy, Marseille (France)
E-mail: laurent.limozin@inserm.fr

[b] Dr. K. Sengupta
CinaM, CNRS UPR 3118
Aix-Marseille University, Luminy, Marseille (France)

que. One of the main reasons is that the interpretation of data is not always straightforward. Herein, we provide a guide to setting up a RIC microscope and interpreting the images. We include examples from fields as diverse as colloid physics, membrane physics and cell adhesion to demonstrate the versatility and capabilities of RICM. We hope that this review will, on the one hand, inspire new users to apply RICM to their specific needs and, on the other hand, serve as a practical guide for existing users and help them in quantitative interpretation of their observations.

Laurent Limozin was born in Marseille in 1972. He did his PhD in Marseille on the modelling of tip-growing cells. In 2000 he moved to Munich for a post-doctoral stay, where he received an Alexander von Humboldt fellowship in the laboratory of Erich Sackmann. During this time, he did pioneering work in developing a technique to manufacture artificial cells by enclosing a synthetic actin cortex inside a giant vesicle, and developed novel techniques to probe the viscoelastic properties of this composite shell. In 2003, he moved back to Marseille as a researcher of Centre National de la Recherche Scientifique, in the laboratory of Pierre Bongrand. Here, he is developing optical surface microscopy techniques, including RICM, coupled to laminar flow chamber for the study of cell adhesion. His current interests include formation and dissociation of single bonds, membrane mechanics and cell adhesion.



Kheya Sengupta was born in Delhi in 1972. She did her PhD in Bangalore with V. A. Raghunathan on liquid-crystalline phases of phospholipids. In 2001 she moved to the laboratory of Erich Sackmann in Munich with an Alexander von Humboldt fellowship. She studied bio-mimetic systems and contributed to the development of multi-wavelength RIC microscopy. In 2004 she moved to University of Pennsylvania, where she worked with Paul Janmey on cell mechanics and cell adhesion. In 2005 she came back to Germany as a research associate at the Forschungszentrum Jülich in the laboratory of Rudolf Merkel, where she continued her work on adhesion and continued to improve RIC microscopy. In 2007 she was offered the position of a researcher of the National Scientific Research Council of France (CNRS) and moved to Marseille. Her current interests include adhesion and mechanical properties of cells and cell mimetic model systems, and the interaction of such soft systems with nanoscale objects.



2. Experimental Set-up

2.1. Typical Equipment

We describe here the standard version of a RICM set-up, which consists of a light source, an inverted microscope equipped with an antilex objective and a CCD camera. The sample is observed under monochromatic epi-illumination. The typical set-up is shown in Figure 1. Variations and add-ons are described below.

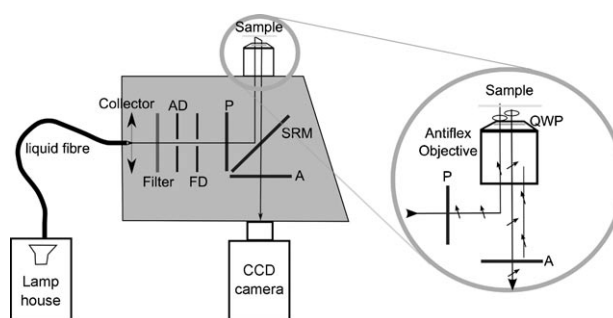


Figure 1. Typical experimental set-up and optical path for a standard RIC microscope. AD: aperture diaphragm; FD: field diaphragm; QWP: quarter-wave plate; SRM: semi-reflecting mirror; P: polarizer; A: analyser. The circular zoom illustrates the polarization of light with the antilex method.

The light source should be incoherent and have sufficient power density at the chosen wavelength. A classical 100 W high-pressure mercury lamp, or modern bulbs offering longer lifetime and more power for similar spectral peaks,¹ are all good choices. The latter is located in a separate unit, connected to the rear entry port of the microscope with a liquid fibre. The advantage of this configuration is that the lamp is pre-adjusted for homogeneous illumination. Additionally, it prevents direct heating of the microscope body, thus reducing the drift of focus—a crucial concern for RICM. When using a classical lamp, manual alignment is necessary to ensure homogeneous illumination. During all adjustments, caution should be taken to avoid direct exposure of the eye.

An inverted microscope is generally used. This is particularly useful for samples where the object of interest has to sediment down to the floor of the observation chamber, as is the case for all the examples presented here. The illumination path inside the microscope includes: a collector at the entrance of the fibre; an interference filter² protected by an anti-caloric filter; and two adjustable diaphragms, namely the aperture diaphragm (AD) and the field diaphragm (FD), which are positioned with respect to the sample and objective to realize a Köhler illumination (see Section 4). The reflector cube in the light path is composed of a polarizer (P), a semi-reflecting mirror (SRM) and a crossed polarizer (analyser, A). The objective

¹ 120 W for the Xcite 120 (Exfo, Canada) and 200 W for the L200 (Prior, UK).

² Usually $\lambda_g = 546 \pm 12$ nm, but other rays of the lamp, such as 436 nm, can also be used.

is specially designed for RICM and includes a built-in quarter-wave plate (QWP) located in front of the front lens. The commercially available option is Neofluar Antiflex (Zeiss). It is of the oil immersion type, with magnification $\times 63$, numerical aperture 1.25 and includes a phase ring for phase-contrast studies. The quarter-wave plate is optimized for a wavelength of 546 nm, which is therefore the recommended wavelength to use in the one-colour set-up.

Currently, the best-suited detection device is a CCD camera, for which several characteristics have to be considered: matrix and pixel size in relation to sample size and magnification; and light detection range of the pixels. Typically, a matrix of 1000×1000 pixels or less and a pixel size of $8 \mu\text{m}$ is used. The capacity of the camera to detect low-light signals is irrelevant on the standard set-up, since the background is grey and should be roughly set in the middle of the detection range. However, the number of grey levels (usually encoded on 8 to 16 bits) is crucial for measurements involving the direct conversion of intensity into substrate-sample separation distance. Finally, modern CCD cameras usually ensure sufficient linearity and sensitivity together with limited noise.

2.2. Typical Samples

In the typical configuration, the sample under study is deposited on a glass cover-slide of refractive index $n_g = 1.525^3$ and immersed in an aqueous medium (water or physiological buffer) of refractive index $n_w = 1.333$. In some cases, the immersing (or outer) buffer may contain additional sugar or proteins, which raises the refractive index to $n_{\text{out}} > n_w$. Herein, the typical objects studied include (see Figure 2):

- micrometre-sized spherical beads of silica ($n \simeq 1.45$), soda lime glass ($n = 1.52$) or latex ($n = 1.59$),
- thin films of liquid, polyelectrolyte, polydimethylsiloxane (PDMS) or supported lipid bilayers, often in addition to beads or vesicles,
- giant unilamellar vesicles of radius 1 to $100 \mu\text{m}$ (bound by a lipid membrane, $n_m = 1.49$), usually filled with a sucrose solution of refractive index n_{in} ,
- animal cells bound by a lipid plasma membrane and of typical lateral extension of 5 to $100 \mu\text{m}$; the cell contains other membranous internal structures or organelles and has a variable total thickness ranging from sub-micrometres to $5\text{--}10 \mu\text{m}$.

3. Theory

3.1. Interferences

The optical basis for interferences occurring in RICM is shown in Figure 3A. A monochromatic incident ray I_0 is first reflected at the glass/medium interface to give the ray I_1 ; the transmit-

³ Thickness $170 \mu\text{m}$ (number 1.5) with especially low thickness variations of $\pm 1 \mu\text{m}$ (available from Assistant Hoechst, Germany).

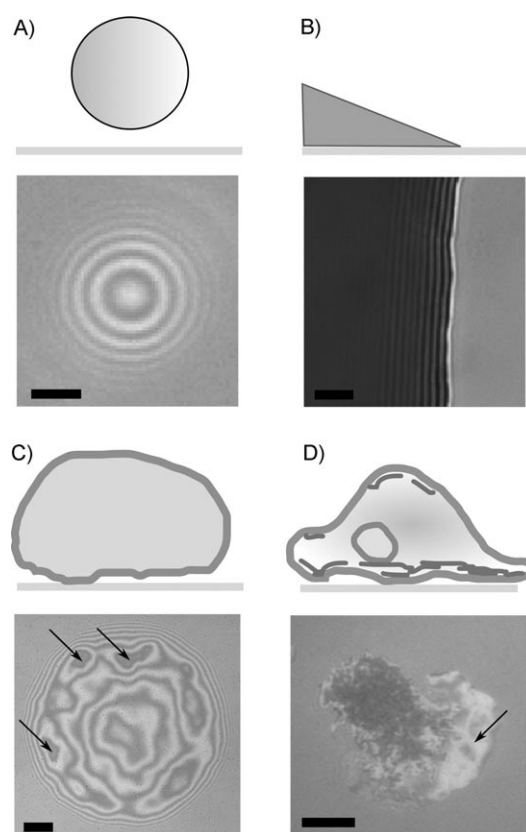


Figure 2. Typical samples: schematic representation of the profile and the RIC micrograph. A) Polystyrene bead ($10 \mu\text{m}$ in diameter) hovering above a substrate. Scale bar: $2 \mu\text{m}$. B) Edge of a millimetre-sized actin-containing droplet. Scale bar: $5 \mu\text{m}$. C) Giant phospholipid vesicle partially adhered to a substrate. Adhesion domains are indicated by arrows. Scale bar: $5 \mu\text{m}$. D) Spreading monocyte with a large lamellipodium indicated by an arrow. Scale bar: $5 \mu\text{m}$.

ted ray is reflected further at the surface of the object and gives rise to the ray I_2 . Rays I_1 and I_2 interfere and give rise to a resultant intensity I , which for quasi-normal incidence is given by [Eq. (1)]:

$$I = I_1 + I_2 + 2\sqrt{I_1 I_2} \cos[2kh(x, y) + \phi] \quad (1)$$

with $k = 2\pi n_1/\lambda$ and ϕ a phase shift usually equal to π . $h(x, y)$ is the distance separating the object and the glass substrate at the lateral position (x, y) . The intensities I_1 and I_2 depend on the incident I_0 as: $I_1 = r_{01}^2 I_0$ and $I_2 = (1 - r_{01}^2) r_{12}^2 I_0$, with the Fresnel reflection coefficient $r_{ij} = \frac{n_i - n_j}{n_i + n_j}$ ($ij = 0, 1, 2$). Therefore, the appearance of contrast in RIC micrographs depends on the last term in Equation (1), which is a function of h .

3.2. Contrast in Reflection and the Antiflex Technique

As seen before, the intensity of the reflected signal depends on the reflection coefficients. The intensity of light reflected in water on soft materials and biological interfaces, such as membranes or polymers, is low. For example, at the water/lipid interface with $n_1 = n_w = 1.333$ and $n_2 = n_{\text{lip}} = 1.486$, $r_{12}^2 = 0.003$, and at the glass/water interface $r_{01}^2 = 0.005$. Therefore, any stray re-

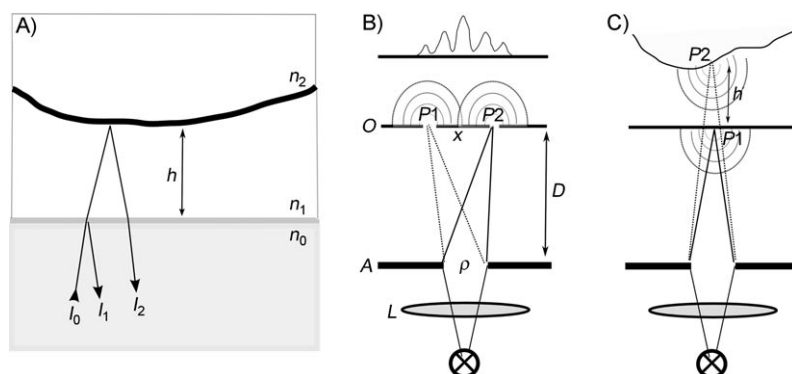


Figure 3. A) Interferences in quasi-normal incidence. B, C) Influence of the illumination aperture (after ref. [9]): B) two pinholes P_1 and P_2 at a distance x are illuminated coherently if $x < x_c = \frac{0.16\lambda}{\text{INA}}$, with $\text{INA} = n\rho/D$; C) in reflection, P_1 and P_2 also act as coherent secondary sources if the object distance h is sufficiently small. (A: aperture; O: object plane; L: lens).

flexion occurring inside the microscope obscures the signal of interest. The antiflex method was designed by Ploem^[2] to overcome this problem and uses the cross polarizers in the microscope reflector combined with the quarter-wave plate included in the antiflex objective (Figure 1, zoom). The incident non-polarized light is rendered linearly polarized after passing through the polarizer. After passing through the quarter-wave plate, it is circularly polarized. In the sample, the circularly polarized light may encounter: 1) interfaces with decreasing refractive index—here the parallel component of the electric field is shifted by π , while the perpendicular component remains unaffected; and 2) interfaces with increasing refractive index—here the perpendicular component of the electric field is shifted by π , while the parallel component remains unaffected. In both cases, the reflected ray, which passes again through the quarter-wave plate, is rendered linearly polarized with a $\pi/2$ orientation shift and passes unperturbed through the analyser. All incident stray light that is reflected before reaching the quarter-wave plate is blocked by the crossed analyser. The contrast obtained from the interferences is measured using the fringe visibility $v = \frac{I_{\max} - I_{\min}}{I_{\max} + I_{\min}}$, where I_{\max} and I_{\min} are respectively the maximal and minimal intensities of the fringe pattern.

3.3. Coherence and Resolution

Up to now, we have considered coherent monochromatic light. In practice, however, the light source is incoherent, not perfectly monochromatic, and presents a certain spatial extension. The theory of partial coherence^[17] states that [Eq. (2)]:

$$I = I_1 + I_2 + 2\sqrt{I_1 I_2} \gamma_{12} \cos[2kh(x, y) + \phi] \quad (2)$$

which defines γ_{12} , the mutual degree of coherence. When considering two rays of equal intensity, the fringe visibility is therefore $v = \gamma_{12}$, and $v = 1$ in the case of purely coherent monochromatic light [see Eq. (1)]. Due to incoherence, only rays coming from the same point of the source can actually interfere. One can therefore define a certain coherently illuminated volume where the optical path difference between rays issued

from the same point source gives rise to a phase difference of less than 1. The size x of this zone, related to the resolution of the technique, can be calculated from the theory of coherence in quasi-monochromatic light. After spectral filtration, the incident light is considered as quasi-monochromatic if the optical path differences considered satisfy $\Delta s \ll \lambda^2/\Delta\lambda = 0.546^2/0.012 \approx 30 \mu\text{m}$, which is mostly true in practice. In Köhler illumination, the source is defined by the aperture diaphragm, which is a disk of radius ρ , small compared to the source–image distance D ;

in the microscope, these quantities are expressed in terms of the illumination numerical aperture (INA) as $\text{INA} = n\rho/D = n\sin\alpha$ where α is the source angular size seen from the sample or, equivalently, the angle of the cone of light emerging from the objective (Figure 3 B,C).

Under these conditions, the Van Cittert–Zernike theorem shows that the mutual degree of coherence is equal to the amplitude of the point spread function $|\gamma_{12}| = \frac{2J_1(v)}{v} \approx \frac{\sin v}{v}$ with $v = \frac{2\pi n \rho x}{\lambda R}$, and J_1 a Bessel function of the first kind. This expression can be understood by considering the interference of light from two pinholes at a distance x from each other and located at a distance D from the source of size ρ (Figure 3 B). Therefore, the volume of coherent illumination defined by $v < 1$ ^[18] corresponds to $x < x_c = \frac{0.16\lambda}{\text{INA}}$. Partial coherence is achieved when $x_c < x < x_{\text{pc}} = \frac{0.5\lambda}{\text{INA}}$. So a high INA imposes a reduced coherence, in particular along the optical axis, which reduces the depth of focus. In the focal plane, each point spreads as an Airy disc of extension scaled by $2\pi\text{NA}/\lambda$, with $\text{NA} = 1.25$ the numerical aperture of the objective. According to the Rayleigh criterion, the lateral resolution is given by half the width of the Airy pattern, which corresponds to $\rho_{\text{ic}} = 0.61\lambda/\text{NA} = 0.264 \mu\text{m}$ for incoherent illumination and $\rho_{\text{co}} = 0.82\lambda/\text{NA} = 0.355 \mu\text{m}$ in coherent illumination. So at low INA, the resolution is given by x_{pc} while at high INA it is given by ρ_{ic} .^[19] The necessity of using an incoherent source now appears clearly: the incoherent illumination imposes that the maximal fringe visibility arises from the region illuminated in the vicinity of the focal plane while other regions of the sample do not contribute to the interferences. Moreover, the size of the region of visibility can be tuned through the INA (see Section 4.2).

3.4. Intensity–Height Relations

3.4.1. Simple Relation

In its simplest form, Equation (1) can be rewritten using the sum S and difference D of the maximal intensity $I_{\max} = I_1 + I_2 + 2\sqrt{I_1 I_2}$ and minimal intensity $I_{\min} = I_1 + I_2 - 2\sqrt{I_1 I_2}$. Using $\phi = \pi$, one finds [Eq. (3)]:

$$2I = S - D \cos\left(\frac{4\pi n_1}{\lambda} h\right) \quad (3)$$

This way of writing Equation (3) is useful since S and D are experimentally measurable quantities.

3.4.2. Effect of Illumination Numerical Aperture (INA)

In RICM, the two pinholes introduced in Figure 3B correspond to the points of first reflection P_1 at the substrate and second reflection P_2 at the object of rays coming from a unique point source (Figure 3C). The mutual degree of coherence γ_{12} is again the amplitude of the point spread function, but calculated this time parallel to the optical axis and is written as $\gamma_{12} = \frac{\sin y}{y} e^{i\phi}$ with $y = 2kh \sin^2(\alpha/2)$.^[17] Inserting this expression in Equation (2) gives the result obtained by Rädler and Sackmann,^[9] which we rewrite here using S and D [Eq. (4)]:

$$2I = S - D \frac{\sin y}{y} \cos\left\{\frac{4\pi n_1}{\lambda} [h(1 - \sin^2(\alpha/2))]\right\} \quad (4)$$

Here α is half the angle of the cone of illumination (Figure 4), which is related to the illumination numerical aperture through $\text{INA} = n_1 \sin \alpha$, and n_1 is the refractive index of the sample medium. Alternatively, the previous expression can be derived by assuming a uniform illumination angle between 0

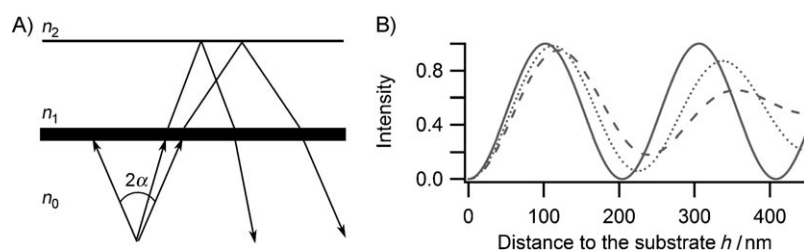


Figure 4. Effect of non-zero illumination numerical aperture (INA) on fringes. A) Incident rays belong to the cone of half angle α . B) Fringes are stretched and damped (.....: $\text{INA} = 0.8$; ----: $\text{INA} = 1$) compared to the reference intensity of Equation (3) [—].

and α and integrating directly the reflected intensity on the angles of incident light.^[9] It compares successfully with the pioneering numerical study of the effect of INA in IRM, by Gingell and Todd.^[20] This expression shows that with increasing INA: 1) the visibility decreases and 2) the fringe spacing is stretched (Figure 4).

3.4.3. Effect of Multiple Interfaces

Up to now, we have considered only one reflecting interface in the object. However, in the case of a vesicle, for example, it is important to account for an additional interface by considering separately the interfaces outer-medium/lipid and lipid/inner-medium (Figure 5A). In this case, the combination of reflected

and refracted rays leads to the reflection [Eq. (5)]:

$$r = r_{01} + (1 - r_{01}^2) e^{4\pi i n_1 d_1 / \lambda} [r_{12} + r_{23} (1 - r_{12}^2) e^{4\pi i n_2 d_2 / \lambda}] \quad (5)$$

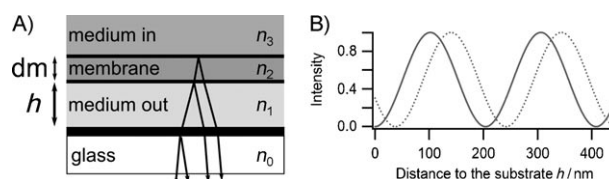


Figure 5. Effect of a triple interface on fringes. A) Refractive indices with triple interface in the case of a membrane hovering above the substrate. B.) Fringes are shifted by a distance h_0 of typically 30 to 40 nm (.....) compared to the reference intensity of Equation (3) (—).

Here $d_1 = h$ is the membrane–substrate distance in the outer medium of index $n_1 = n_{\text{out}}$ and $d_2 = d_m \simeq 4$ nm is the membrane thickness of index $n_2 = n_m \simeq 1.49$.^[9] This leads to a shift h_0 in the fringes (Figure 5B) which are given by [Eq. (6)]:

$$2I = S - 2D \cos\{2k[h(x,y) - h_0]\} \quad (6)$$

where $h_0 = -\frac{\lambda}{4\pi n_{\text{out}}} \arctan \frac{\gamma \sin \delta}{1 + \gamma \cos \delta}$ with $\gamma = \frac{r_{23}}{r_{12}} (1 - r_{12}^2)$ and $\delta = 4\pi n_m d_m / \lambda$.^[12] Therefore the shift depends on the refractive index of both inner and outer media.

3.4.4. Effect of Tilted or Curved Interfaces

In the preceding sections, it was implicitly assumed that the reflecting interfaces are planar and perpendicular to the optical axis. However, if the normal to an interface is tilted with respect to the optical axis or if an interface is curved, reflected rays will be displaced laterally compared to their position of incidence. The case of a sphere is illustrated in Figure 6A. To quantify this effect

on the fringe pattern, one has to trace back and sum the contribution of all the reflected rays reaching a given point of the image plane.^[21,22] The radial profile of intensity obtained numerically in the case of a sphere is shown in Figure 6B (.....). (—) is the radial profile obtained for the same sphere, but using Equation (3) and describing the surface of a sphere as a succession of infinitely small horizontal segments, on which light arrives and is reflected parallel to the optical axis. A tilted interface induces a reduction of the inter-fringe distance. Due to the lateral resolution of the microscope, the fringes are visible as long as the slope of the interface $\partial h / \partial x$ is less than the maximal slope $\partial h / \partial x|_{\text{max}} = n/n_0(\text{NA} - \text{INA})$.^[9]

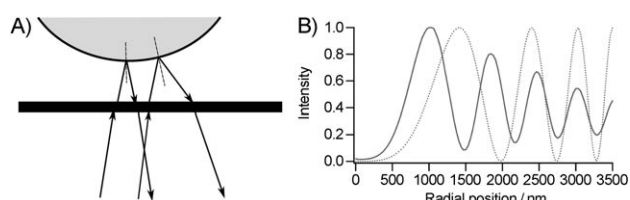


Figure 6. Effect on the fringes of a curved interface. A) Reflected rays are shifted away from the vertical axis of a bead. B) Fringes calculated for a spherical bead of radius 5 μm at a distance 1 nm from the substrate: assuming normal incidence on a surface segmented in horizontal steps (.....) or taking into account the deflection of rays by the curved interface, with $\text{INA} = 0.1$ (—).

3.5. Dual-Wave RICM

One major drawback of the conventional mono-wavelength RICM discussed so far is that the information about the phases of the beams reflected by the various interfaces of a film is not known. In other words, from Equation (3) it is clear that the intensity is a function of the height modulo a factor $\lambda/2n$ (where λ is the wavelength of the incident light and n is the refractive index of the medium). This repetition of the fringe pattern is well known in any interference phenomena. In the context of RICM with green illumination, it means that unless it is clearly established that the object in question (or a part of it) is closer to the substrate than 100 nm, the height cannot be determined unambiguously from the intensity (Figure 7A). In the

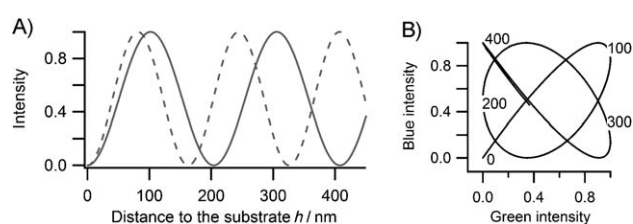


Figure 7. Dual-wavelength RICM. A) A single wavelength (green, —) does not permit the unambiguous retrieval of the height from a measurement of the intensity. Usage of a second wavelength (blue, ----) lifts the ambiguity for h up to 800 nm. B) Variation of the blue intensity as a function of the green intensity with h as a parameter is used to determine h . Equivalently, the curve is obtained using Equation (7).

context of cell or vesicle adhesion, this requirement is often fulfilled since the adhering membrane is necessarily at the surface. In the case of freely fluctuating membranes or colloidal beads, however, there may often be an ambiguity about the phase factor of the cosine defining the height/intensity relationship. This drawback can be overcome by dual-wave RICM, which compares the interferograms obtained simultaneously at two different wavelengths (Figure 7A). The additional periodicity and boundary condition introduced by observing a second wavelength lifts the ambiguity and enables the measurement of the absolute height of an object above a planar surface.^[10,23,24]

From Equation (3), if the information about the intensities I^g and I^b ($g = \text{green}$, $b = \text{blue}$) is available for two wavelengths λ^g

and λ^b , respectively, I^b can be expressed as a function of I^g [Eq. (7)]:

$$I^b = D^g - S^b \cos\left(\frac{\lambda^g}{\lambda^b}\right) \arccos\left(\frac{D^b - I^g}{S^g}\right) \quad (7)$$

where $D^{g,b} = I_{\text{max}}^{g,b} - I_{\text{min}}^{g,b}$, $S_{g,b} = I_{\text{max}}^{g,b} + I_{\text{min}}^{g,b}$, and the subscripts max and min denote the maximum and minimum intensity, respectively. A parametric plot of I^g and I^b (Figure 7B) demonstrates that a unique height can be assigned to every given pair of values I^g and I^b .

The particular choice of λ^g and λ^b pushes up the range of unambiguous height determination to about 800 nm. However, in principle, any combination of multiple wavelengths can be used.^[10,25] In this case, the range of height determination is limited only by the depth of focus.

4. Practical Hints and Alternative Set-ups

Based on the previously developed theoretical bases, in this section we present some practical aspects of the use of RICM. We also briefly describe the implementation of dual-wave RICM and the combination of RICM with fluorescence.

4.1. Köhler Illumination

Implementing a proper Köhler illumination ensures that all the optical elements are oriented and centred correctly with respect to the light path. While the Köhler adjustment for transmitted light is often explained in manuals for advanced microscopy, the adjustment for reflected light is usually ignored. The principle is, however, the same, except that in the case of reflected light microscopy, the aperture diaphragm is placed right after the source/condenser and the field diaphragm is placed between the aperture diaphragm and the objective (Figure 1^[18]). As in transmission microscopy, Köhler adjustment ensures that: 1) when the object is in focus, the aperture diaphragm is conjugate to the exit pupil of the objective and the field diaphragm is conjugate to the object plane; 2) both the diaphragms are perpendicular to the incident light beam; and 3) both the diaphragms are properly centred. In epi-illumination on an inverted microscope, the first two conditions are usually fixed by the microscope manufacturer. To fulfil condition (3) for the field diaphragm, it is usually sufficient to centre it visually. To centre the aperture diaphragm, it is very useful to be able to look directly at the exit pupil of the objective. This can be achieved either with the help of a Bertrand lens or simply by removing one of the oculars and looking through the ocular tube. One can then see two concentric rings that in fact arise from the phase ring built into the antireflective objective. The opening of the aperture diaphragm is also directly seen and it can be centred easily with respect to the phase ring. To achieve finer adjustment, the ocular is replaced and the object is slightly defocused; if the image of the object does not shift but simply dilates, the aperture diaphragm is properly centred. If not, its position can be slightly adjusted to bring the image back to its original position. This has to be done repeatedly

untill defocusing no longer shifts the image. At this point, Köhler illumination is properly achieved.

4.2. Using the Aperture Diaphragm

In epi-illumination for fluorescence, the correct choice for the opening of the aperture diaphragm (INA, see Section 3.3) corresponds to the numerical aperture of the exit pupil of the objective. However, in RICM, the choice of the INA is dictated by other considerations. Here, the illumination angle determines how close the set-up is to the case of perpendicular incidence. Thus, if the simple formula [Eq. (3)] is to be used for data analysis, it is imperative to keep the INA as small (point-like) as possible. The other consideration is the depth of field. As in any microscopy, the smaller the illumination angle, the larger is the depth of focus, as explained in Section 3.3. Therefore, if the experiment requires a large depth of field, for example to reconstitute the height of an object up to a couple of micrometres above the substrate, the INA should be kept small. This is often the case while working with beads or when the fluctuations of the membrane of a very floppy vesicle are to be measured. However, if the object of interest lies close to the substrate, it is sometimes better to use a large INA for two reasons. Firstly, a large INA improves the lateral resolution. Secondly, a smaller depth of focus means that the light is rendered incoherent before it travels far into the substrate. Thus, if the object is thin and there may be a second reflection from the upper surface, as is often the case with cells, a large INA may avoid the problems arising from multiple reflections. For this reason, in cell work, a high INA is usually recommended.⁴

4.3. Adjusting the Quarter-Wave Plate, Uniformity of Field and Focusing with the Field Diaphragm

Clearly, to be effective, the quarter-wave plate needs to be oriented correctly (axis at 45° with respect to the direction of polarization). To achieve this, after adjusting the INA to a closed position, the quarter-wave plate should be rotated (with the help of the collar near the top of the antireflective objective) until the field of view is maximally illuminated. Simultaneously, halos arising from undesirable reflections should be strongly reduced.

Since in RICM the intensity information is used for quantitative analysis, it is very important to achieve uniform and homogeneous illumination over the entire field. If the microscope is well adjusted as described above, including the lamp positioning, the main source of inhomogeneous illumination arises from a tilt of the sample holder with respect to the focal plane of the objective. This problem can be easily detected by checking whether or not the image of the field diaphragm is sharply in focus all along its periphery. If not, the sample holder has to be rendered horizontal^[11] by using adjusting screws and test-

ing the sharpness of the field diaphragm at different points of its circumference. For high-precision measurement, the field diaphragm should be perfectly in focus. This can be achieved by using a piezoelectric element placed under the objective, to move the objective vertically on a short range around the focal position and record images simultaneously. The position at which the diaphragm appears the sharpest corresponds to the focus. An easy way to measure the sharpness is to fit a sigmoidal curve to an intensity profile taken perpendicular to the diaphragm image. A precision of the order of 10 nm is achieved using this method at high INA.^[11] Alternatively, the variance of the image of a portion of the diaphragm can be monitored^[16] or a bead attached to the substrate can serve as reference for an autofocus.^[26]

4.4. Camera Specifications and Settings

Dynamic range, exposure time and noise are important concerns for quantitative RICM performance. For recording, a CCD camera with sufficient dynamic range must be chosen. The maximal resolution δI in intensity measurement is related to the number of grey levels N_{gl} by $\delta I = (I_{\text{max}} - I_{\text{min}}) / N_{\text{gl}}$ assuming that the full range is used. $N_{\text{gl}} = 2^n$, with n the bit depth of the camera, usually 8 to 16. Unlike in fluorescence, the feebleness of illumination is usually not an issue. However, since fast dynamical processes are often studied, it is interesting to reduce the exposure time as much as possible. However, a reduced exposure time decreases the signal-to-noise ratio, which directly affects the precision of the measurement. This can be partly compensated for either by increasing the illumination through the aperture diaphragm (with the consequences discussed in the previous paragraph), or by applying an image treatment (see Section 5). In studies of time-dependent fluctuations where the intensity is directly transformed into height, another concern enters the picture—that of the shot noise of the camera which increases as the square root of the intensity.^[58]

4.5. Combination with Fluorescence and Dual-Wave RICM

RICM can easily be combined with other techniques, such as epifluorescence or bright-field/phase-contrast in transmission. In the case of bright field, two different incident wavelengths have to be used for the two techniques. In the case of fluorescence, if the dye is chosen appropriately, a single incident wavelength can be used for both the techniques. The polarizing filter cube is placed in the filter wheel to take advantage of the antireflective technique. The reflected light contains both the RIC signal and the fluorescence signal. These are separated using a filter cube appropriate for the fluorescent dye used just before the light enters the camera. Alternatively, a dual-band filter may be used to illuminate the sample with one wavelength being used for RICM and the other for fluorescence. The subsequent set-up remains the same, except that the choice of filters may have to be modified. Since the amplitude of the recorded signals for RICM and fluorescence may differ by orders of magnitude, care has to be taken to ensure that the emission wavelength and the RICM wavelengths are

⁴ To quantitatively account for the INA and make use of Equation (4), the INA has to be measured. This can be done by tracing the cone of light emerging from the objective by placing transparent blocks in place of the sample and marking the diameter of the cone on each block. The INA is related to the half-angle α of this cone, which is the cone of illumination, by $\text{INA} = n \sin \alpha$.

well separated in the spectrum. A similar set-up can be used to implement dual-wave RICM. A dual-band filter is introduced into the path of the incident light. An additional separation of colours may be required in the reflected/emitted light path. This is effected using filters and/or dichroic mirrors just before the light enters the camera(s).

An issue that has to be resolved in any multi-wavelength work using the antiflex objective is that of chromatic aberration. The commercially available antiflex objective is of the type "plan-Neofluar" and is therefore capable of forming high-quality images in monochrome. However, in practice it gives rise to the problem that the focal planes of the different wavelengths differ. For example, the plane of focus of the blue wavelength is displaced by as much as 0.6 μm from the plane of focus of the green wavelength.

Two specific implementations can be envisaged for multi-wavelength applications, which address the issue of chromatic aberration. In the first implementation, two separate cameras are used for the two wavelengths,^[10] and their positions are adjusted such that the image is focused correctly for each. A convenient device is a dual video adapter (Zeiss, Germany) which can be used to separate the two wavelengths.^[27] The two cameras can be coupled electronically in such a way that one signal suffices to activate both,^[27] thus ensuring perfectly simultaneous recording. A less precise alternative is to activate the two cameras independently. The small time lag thus introduced has to be then corrected for during the data analysis stage by comparing the in-plane trajectories of moving objects recorded by the two cameras and demanding that they overlap perfectly.^[10]

The alternative to using two cameras is to use a single camera that images both channels. In this case, it is necessary to implement a semi-automated focusing system using, for example, a motorized microscope so that the objective can be driven automatically over a predetermined distance to focus alternately at the relevant focal planes. The colours can be separated either by use of a colour camera or by introducing appropriate filters in the light path in a synchronous fashion.

4.6. IRM versus RICM

Originally, Curtis introduced the interferometric measurement of cell-to-substrate distance under the name "interference reflection microscopy" or IRM.^[1] The crucial difference with RICM is that the antiflex method, which considerably improves the contrast (see Section 3) is not used. In many biological applications, IRM is still preferred over RICM, perhaps because the antiflex objective is commercially available from only one company and for one choice of magnification (Section 2). In addition to offering a poorer contrast, the precise intensity/height relationship, which accounts for polarization effects, is also different for IRM and RICM. While IRM can be used for qualitative diagnosis of close contact, for quantitative application where it is desirable to explicitly measure the cell-to-substrate distance from the intensity, it is imperative to use a correctly adjusted RICM set-up.

5. Image Treatment and Height Reconstruction

To fully exploit the potential of the data for quantitative measurements, RICM requires careful image treatment and analysis. In this section, we first discuss the pre-treatment necessary before the intensity information in the image can be converted to height. We then discuss the estimation of the errors involved in the height reconstruction process and finally explain in detail the height reconstruction procedure for different kinds of samples.

5.1. Heterogeneity of the Background and Reference Intensity

Even when all the instrumental adjustments are done properly as described before, the illumination is, often, still not perfectly homogeneous. To correct for that at the image analysis stage, a robust and easily implemented protocol consists of the following: the pixels in the image that correspond to the object (bead/vesicle/cell) are masked and a planar parabola is fitted to the background. The fitted parameters are then used to generate a theoretical image of the non-uniform background and this background is subtracted from the entire image.^[12]

Another source of error arises from temporal variations in the illumination intensity. It is a fact of life for the microscopist that the best of lamps fluctuates in time. Fortunately, for most purposes it is sufficient to work with relative and not absolute intensities. In principle, for RICM work, it would be necessary to monitor the incident intensity, for example by inserting a diode into the incident light path. A way around implementing this extra hardware is to use the average background intensity as a reference;^[12] more details are given in the following section.

5.2. Height Reconstruction and Normalization of Intensity

The intensity versus height relations and their applicability has already been discussed in Section 3. Below, we explain how these equations have to be applied to real experimental data.

5.2.1. The Min/Max Method

Often, for example for a fluctuating colloidal bead or a membrane that spans all heights between 0 and a couple of hundred nanometres, the information about the quantities S and D in Equation (3) can be extracted with relative ease from experimental data. If I_M and I_m are the maximum and minimum intensities in the experimental fringe pattern that can be read off by a simple algorithm, and the INA is low such that a quasi-normal incidence can be assumed, for a planar interface, $I_M = I_{\max}$ and $I_m = I_{\min}$ where I_{\max} and I_{\min} are the theoretical maximum and minimum of the intensity (defined in Section 3.4.1). In this case, the substrate/object distance h can be determined directly [Eq. (8)].^[28]

$$\frac{2I - (I_M + I_m)}{I_M - I_m} = \cos\left(4\pi n \frac{h}{\lambda}\right) \quad (8)$$

where n is the refractive index of the outer medium and λ is the wavelength of the incident light. In practice, to correctly identify I_M and I_m , it is necessary to look at an image sequence rather than a single snapshot. Care must be taken to ensure that scattering from surface defects or dirt or the camera noise does not dominate the determination of I_M and I_m . We call this the min/max method.

As is evident from Equation (8), an important question is which branch of the cosine function to use. In the case of a partially adherent membrane, it is clear that the adhered part belongs to the first branch. Assuming that the membrane height increases smoothly and continuously, one can assign the values 2,3,4... to the subsequent fringes and choose the correct branch accordingly. Alternatively, the branch can be determined using dual-wave RICM (Section 3.5).

If INA is large, the approximation of quasi-normal incidence no longer holds and the experimentally determined maximum and minimum intensities cannot be directly used to determine h . Also, if reflections from multiple interfaces are important, in the light of Section 3.4, the min/max method cannot account for the phase shift factor and correctly measures only relative heights, not absolute heights. However, if INA is known, one can, in principle, relate the observed minimal and maximal intensity I_m and I_M with the values I_{\min} and I_{\max} by using Equation (4).

5.2.2. The Refractive Index Method

In the case where reflections from multiple interfaces are important or the object of interest does not span all the heights between 0 and a couple of hundred nanometres, the min/max method cannot be used. In this case, if the refractive indices of the reflecting media are known, Equation (1), written in terms of the Fresnel reflection coefficients, can be used to determine the substrate/object distance h . In this approach, first the theoretically expected intensity curve I_{th} is generated using Equation (6).⁵ This curve is normalized with respect to the expected background intensity I_0 . Finally, following Equation (5), the normalized intensity curve is of the form [Eq. (9)]:

$$\frac{I_{\text{th}} - I_0}{I_0} = Y_0 - R_0 \cos\left(4\pi n \frac{h - h_0}{\lambda}\right) \quad (9)$$

where Y_0 , R_0 and h_0 are constants which are related to the refractive index of the medium. These constants can either be computed analytically using Equation (5)^[12], or a numerically generated intensity curve is fitted with Equation (9) to obtain the constants. The most important amongst these is the phase-shift factor h_0 . Next, the intensity data are normalized

⁵ This equation is written for three reflecting interfaces, as is the case with a vesicle close to a base glass substrate. This can be generalized to any number of interfaces.^[9,14]

with respect to the measured background intensity. Finally, h is found for every I by inverting Equation (9). We call this the refractive index method. As in the min/max method, we need to determine which branch of the cosine to use for determining h . With the introduction of the phase-shift factor h_0 , there is a 0th branch added to the cosine wave spanning $h=0$ to $h=h_0$.

If INA is large, as before, the procedure described above cannot be used directly. In this case, one possible approach is to carry out the normalization of each branch of the cosine separately. Accordingly, first the theoretically expected intensity curve, calculated following the procedure described above and modified to account for the large INA [Figure 4 or Eq. (4)], is normalized branch-wise so that the maximum and minimum for each branch are at 1 and 0, respectively. Next, the experimental intensity curve is normalized similarly and is compared to the theoretical curve. Finally, the height corresponding to each intensity is read off.

5.3. Absolute and Relative Height Determination

In the preceding sections, intensity/height relations were developed where the height h is the height of the object measured from the surface of the substrate. In other words, RICM can, in principle, measure absolute heights. For many applications, however, it is sufficient to measure the relative height. For example, in the case of a fluctuating bead, it may be enough to know the increment in height from one time frame to the next or in the case of an adhering vesicle, the quantity of interest may be the shape of the membrane and not its absolute location above the substrate. In fact, practically, absolute height measurements are less reliable than relative height measurements. The former requires knowledge of all the refractive indices, whereas for the latter, since in general the refractive index of the medium is known, a precise knowledge of other refractive indices is not required as long as they do not change significantly during the observation period.

5.4. Colloids—Height Reconstruction with Known Symmetric Shape

As can be appreciated from Sections 3 and 4, measuring and comparing absolute intensities is a delicate operation. In the context of RICM, if the geometry of the object to be observed is known, this knowledge can often be exploited to devise an alternative to height determination from the intensity. Such a symmetry-based analysis is often more robust than an analysis based on quantification of the intensity.

In the context of colloidal beads, the known geometry of the object is spherical. Therefore it is expected to give rise to fringes with circular symmetry. The RICM image of a bead hovering over a planar substrate consists of a concentric array of circular interference fringes (Figure 2A). A change in the height of the bead changes this fringe pattern in a systematic manner, as illustrated in Figure 8.

From considerations of geometrical optics, for a bead of radius R , the relation between the height h and the radius r_l of the l th interference ring can be written in a simple form

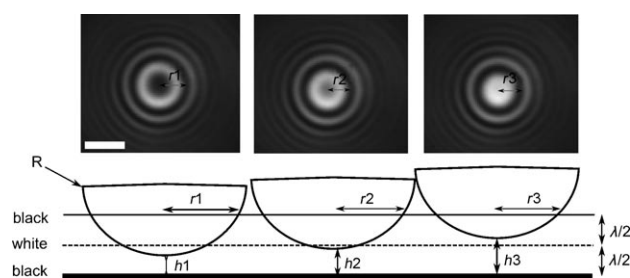


Figure 8. Top row: RICM fringe pattern arising from a colloidal bead that changes its height h above a substrate from $h=h_1$ with $h_1 < \lambda/2$ to $h=h_2$ with $h_2 \approx \lambda/2$, and finally to $h=h_3$ with $h_3 > \lambda/2$. The intensity at the centre of the innermost fringe changes; meanwhile the radius r of the first dark ring-like fringe changes too so that $r_1 < r_2 < r_3$. Scale bar: 2 μm . Bottom row: schematic of the bead profile. The solid line at $h=\lambda$ represents the height at which a fringe looks dark: the dark fringes above are the line of equal height with $h=\lambda$. As the bead height changes, the bead profile is intersected by this line at different levels and thus the radial cross section r changes.

[Eq. (10)]:^[10]

$$h(r_i) = \frac{\lambda l}{2n} - R + \sqrt{R^2 - r_i^2} \quad (10)$$

This expression, however, proves to be inadequate since neither the illumination aperture nor the curvature of the bead is taken into account. One way around this is to perform calibration experiments to construct, for a given R , an empirical relation between h , as calculated from the intensity using Equation (8), and r_i , as measured from the pattern. This empirical relationship is then used to determine the height of the beads directly from r_i in subsequent experiments. Using this technique, the absolute and relative heights of a bead can be determined with an accuracy of 3 and 0.4 nm, respectively. This procedure can be generalized to a size-independent calibration, which was implemented using an atomic force microscope to precisely position beads of different known sizes over substrates at known heights and recording the corresponding RICM pattern.^[11] The calibration curves were prepared from measurements of r_i for two different values of l for each known value of h and R . In the real experiment, measurement of the radii of two different fringes enables the determination of the two unknown parameters h and R by comparison with the calibration curves. This method has the advantage of being model independent but has the disadvantage of being dependent on the fine-tuning of the microscope. In both procedures, the symmetry of the fringes arising from the beads is simultaneously exploited for determination of the lateral position of the centre of the beads with sub-pixel accuracy.^[11]

The height determination using fringes is very robust, but it does not overcome the limitations of mono-wavelength RICM. In certain conditions, the amplitude of bead fluctuations gives an indication of the proximity of the surface. However, to determine the absolute height in the general case, the dual-wave approach of Section 3.5 and Figure 7 has to be adopted. In practice, often the quality of data obtained from the green wavelength is superior to that obtained from the blue, since the green line of mercury (the standard illumination) is stron-

ger than the blue and the quarter-wave plate is optimized for green. Therefore, it is often convenient to first determine the height of the bead from the fringe pattern obtained from the green illumination using the fringe method described above, modulo the phase factor $\frac{\lambda}{2p}$ and then to cross-check the blue intensity to assign the appropriate value to l .

The main error in height determination for beads comes from the structure of the beads themselves. Polystyrene beads, which are commercially available and relatively easy to use for most applications, have a fuzzy rather than hard surface. This means that the optical interface is rather ill defined. Thus, measuring the height of beads seemingly stuck to a glass surface can yield non-zero values for the height.^[11,24] Using glass beads or specially designed polystyrene beads (sulfate terminated, rather than carboxyl terminated) improves the measurement. However, in light of Section 5.3, it is clear that only the absolute height determination is affected by this problem, and the accuracy of the relative height determination remains mostly sufficient.

5.5. Model Membranes—Height Reconstruction with Unknown Shape

A free, small, and tense vesicle has the same spherical geometry as a colloidal bead and can be treated in the manner as described above. However, if such a vesicle undergoes deformation, for example due to adhesion, or if one considers the floppy membrane of a flaccid giant vesicle, the symmetry considerations are no longer valid. In this case, there is no alternative to an intensity-based analysis. Classically, Equation (8) was used to determine the topography of a membrane above a substrate.^[28,29] This is adequate if the refractive index of the buffer filling the interior of the vesicle is approximately equal to the refractive index of the vesicle membrane. However, often the vesicle is filled with a buffer whose refractive index is considerably lower than that of the membrane. In this case, the membrane has to be treated as a layer of finite thickness and Equation (9), which takes into account the additional reflection from the membrane, must be used.

As can be seen from Equation (9) and Figure 9A, accounting for the extra reflection introduces a phase shift in the interference pattern. One concrete consequence of this is that tightly adhering vesicles exhibit a dark ring around the adhesion disc (Figure 9B). This ring represents the line of equal height corresponding to $h=h_0$ which occurs typically at about $h=36$ nm (typical values of refractive indices used in giant unilamellar vesicle (GUV) adhesion assays: $n_{\text{in}}=1.34$, $n_{\text{out}}=1.33$). We refer to this line as the “dark rim”. The presence of the dark rim offers the practical advantage that it can be used to delimit the parts of the membrane where the height has to be evaluated in the 0th fringe (Figure 9A), and is therefore below h_0 , from the parts where it must be determined from the first fringe. Another consequence is that within the adhesion disc, the parts of the membrane that are close to the height h_0 appear darker than the tightly adhering parts of the membrane at a lower height. An example is seen in Figure 9C,

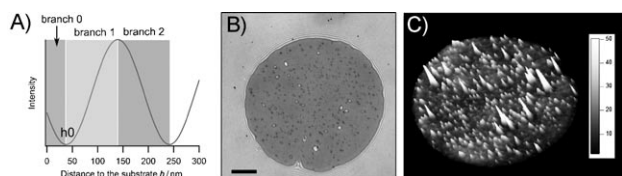


Figure 9. A) Cosine function that represents the intensity versus height relationship, which shows a phase shift h_0 with respect to the expectations from simple theory. This implies that the lowest heights have to be determined in the branch marked "0" and those between h_0 and the first bright fringe have to be determined in the branch marked "1". B) RIC micrograph of a vesicle adhering tightly to a substrate. Note the black rim around the adhesion disc that arises as a consequence of the phase shift. C) Topography of the adhesion disc reconstructed from (B).

where the dark pockmarks are now correctly identified as elevated blisters.

5.6. Cell Membranes—Height Reconstruction with Unknown Shape and Unknown Refractive Index

As a first approximation, the refractive index of the intracellular material can vary between 1.36 and 1.40.^[3] Therefore, from the discussion above, dark zones in RICM can be expected to correspond to the areas where the membrane is close to the substrate. Usually, the closer the membrane is to the substrate, the darker is the corresponding area in the image. Therefore, the tightly adhered areas of the cell show up as dark patches in RICM. Often the simple detection of a dark patch can be taken as a signature of tight adhesion. However, it must be noted that unlike vesicles, a cell is rather inhomogeneous with respect to its internal refractive index; local variations of membrane composition or the presence of internal structures, for example stress fibres close to the membrane,^[3] may change either the refractive index of the membrane or the local internal bulk refractive index. Moreover, there may be extra reflections from internal membrane-bound structures such as the nucleus. For certain cell types, for instance neutrophils, there may be considerable surface roughness, for example due to the presence of microvilli that scatter, rather than reflect, light.^[30] Another consideration that is important while interpreting RIC images from cells is the possibility of a second reflection from the upper membrane of the cell^[3,5] (see, for example, the lamellipodia in Figure 2D). A particularly striking example is that of a red blood cell for which, after adhesion, strong fringes can be seen due to reflection from the upper membrane of the cell even though the lower membrane is tightly bound.^[31] For all these reasons Equations (8) or (9), developed for smooth homogeneous membranes, cannot be applied, strictly speaking, to cells. As an alternative to asserting a precise relationship between I and h , a semi-quantitative description may be adapted which distinguishes between "adhered" and "non-adhered" parts of the cell membrane, where "adhered" is less than 40 nm⁶ from the surface and "non-adhered" is further away. This criterion of dark/bright is easy to

⁶ 40 nm is an chosen rather arbitrarily since it is a little less than half way to the maximum which occurs at 100 nm.

implement by eye, but a quantitative and robust implementation in a numerical algorithm requires some care and is described next by taking a spreading neutrophil as an example.

In a RIC micrograph, a partially spread neutrophil appears as a patchy grey and black area in a uniformly grey background (Figure 10A). Therefore, a simple intensity threshold algorithm

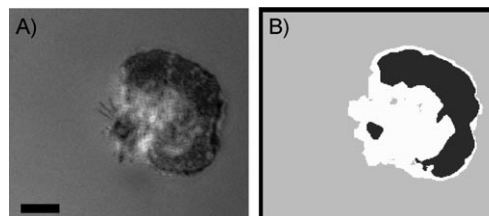


Figure 10. A) RIC micrograph of a partially spread neutrophil. Scale bar: 5 μm . B) The corresponding binary image marking out the cell body and the tight adhesion patches.

is not enough to identify the cell boundaries, since it contains both brighter and darker than average intensities. To identify simultaneously the boundaries of the cell and the adhesion zones inside it, we exploit the fact that the intensity of the background is more uniform than the intensity of the cell. In other words, the spread in intensity of the background is narrower than the spread in intensity within the cell. Application of a simple variance filter⁷ shows that this operation alone is not sufficient in the present case to identify the cell spread area, since the well-adhered parts of the cell membrane are uniformly dark. Thus, a combination of a variance filter to identify the non-adhering parts and an intensity threshold to identify the adhered areas has to be used.^[30] The intensity threshold can be easily identified by constructing a histogram of the entire RIC micrograph. The peak of the histogram of course corresponds to the grey background intensity. Careful inspection reveals a second peak, situated to the left of the main peak, which corresponds to the darker adhered area. This value can be used as the intensity threshold. Using the variance threshold and the intensity threshold criteria, an image is obtained where three distinct regions, namely the background, the cell body and the dark adhesion zones, are clearly marked out (Figure 10B). In case a time-dependent process such as cell spreading is observed, the thresholds determined for one snapshot can be consistently used to evaluate the entire RICM sequence.^[30]

It is clear from the above discussion that the main error in height determination in cells comes from the lack of an independent measurement of the refractive index which may, in addition, vary with time, for example with the movement of intracellular organelles. However, if we are interested in relatively fast processes that induce limited intensity variations, such as membrane fluctuation, it may be safe to assume that the re-

⁷ An $m \times m$ variance filter acts on the original image in such a way that it constructs an "s.d. image" where each pixel contains information about the standard deviation of intensities contained in an $m \times m$ matrix centred on the given pixel.

fractive index changes much more slowly than the height. In this case, in light of Section 5.3, the relative height measurements remain reliable.

6. Applications

In this section we try to give a flavour of the power of RICM in the context of a few recent scientific advances.

6.1. Colloidal Probes

6.1.1. Bead Tracking and Surface Mapping

The procedure described in Section 5.4 yields the trajectory of the colloidal bead under study with 10 nm lateral and around 5 nm vertical resolution, depending on the state of the bead surface (see Sections 5.3 and 5.4). Such a trajectory can be exploited to map the topography of the surface on which the bead sits^[10,11,23] (Figure 11). Recently, simultaneous tracking of a population of beads has been implemented; this enables rapid tri-dimensional mapping of an entire surface.^[11,32] Another interesting application is the tracking of beads undergoing sedimentation. Using this technique, Stoke's law was shown to be applicable at the micrometre scale.^[10] An intriguing possibility for further exploitation of the technique is to measure deviations in bead trajectories to detect very dilute layers, of graft-

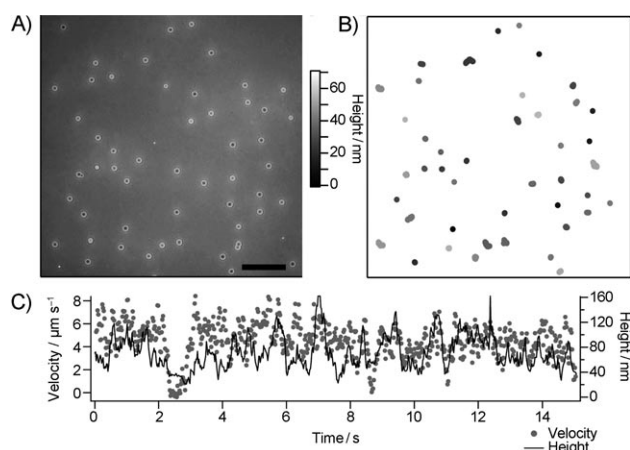


Figure 11. A) RIC micrograph of an ensemble of 5 μm silica beads sedimented on a polymer-coated surface. Scale bar: 10 μm . B) Tri-dimensional positions of the same beads retrieved from fringe analysis. C) Time-dependent height and velocity of a 5 μm silica bead in a laminar flow.

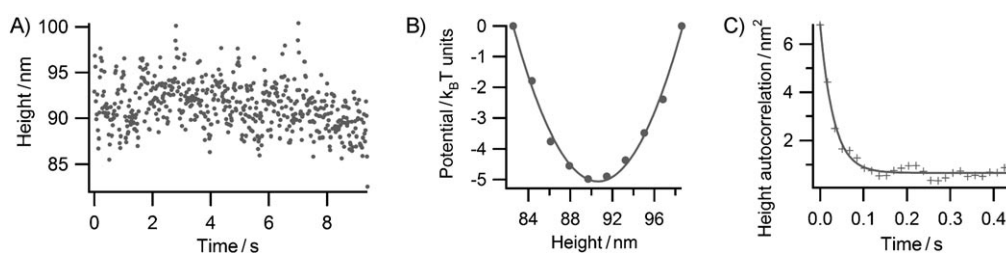


Figure 12. A) Height trace of a colloidal bead hovering over a polymer layer. B) The potential in which the bead resides, as calculated from the height trace using the Boltzmann equation. (●) represent data points and the line is their fit to a parabola. C) Height autocorrelation fitted with an exponentially decaying function.

ed polymers for example, which interact very weakly with the probes.

6.1.2. Colloidal Bead Rheology

In many soft systems the system configurations can be observed and recorded directly, and therefore a fascinating possibility arises: the interaction potential can be computed from direct observation of the number of states being accessed.^[33] With RICM, the in-plane and out-of-plane positions of colloidal probes can be measured with sufficient accuracy to exploit the above possibility.^[21,23,24,34,35] To achieve this, first the height of the bead is traced over time using the methods of Section 5.4 (Figure 12A). This height trace is then binned to construct the probability distribution of the heights—as expected for an object undergoing thermal fluctuations at the minima of a well-defined potential, the probability distribution is, to a good approximation, a Gaussian function. To construct the potential, one can use the Boltzmann equation $V(h) = k_B T \ln[P(h)]$, where k_B is the Boltzmann constant, T is the temperature, $V(h)$ is the potential and $P(h)$ the probability distribution of the accessible states (Figure 12B). In a similar spirit, the height autocorrelation function can be exploited with the help of the Langevin equation to measure the friction γ experienced by the bead according to: $\langle h(t)h(t + \tau) \rangle_t = \frac{k_B T}{V''} e^{-\tau/\tau_0}$ where $V'' = d^2V/dh^2$, and $\tau_0 = \frac{\gamma}{V''}$ is the measured relaxation time (Figure 12C).

If the colloidal probe rests on a polymer cushion, the stiffness of the interaction potential V'' and the friction coefficient γ can be related to the viscoelastic properties of the polymer. This colloidal probe rheology is a facile technique for measuring the viscoelasticity of thin films of soft materials. With this technique, the elasticity of surface-grafted hyaluronan was measured to be as low as 2 Pa.^[23] The technique has also been applied to polyelectrolyte multi-layers.^[11,24,36] The force involved here is the weight of the bead, of the order of 0.1 pN.^[11] Therefore, this technique is particularly suitable when the polymer is too soft to be probed by techniques such as atomic force microscopy, in which forces of the order of 10 pN or more are exerted.

6.1.3. Single Molecules Probed Using Flow

Recently, RICM has been used to study the motion of colloids in a laminar flow. Tri-dimensional trajectories were segmented in superposed layers parallel to the substrate and were ana-

lysed to measure the height-dependent transport properties. It was shown that the long-predicted laws for the diffusion of a sphere in the vicinity of a wall were valid.^[11] Additionally, the laminar flow was used to detect the formation and detachment of the single bond formed between antibodies attached to the beads and antigens linked to the substrate. It was shown that in the presence of a hyaluronan coating, the thickness of the polymeric layer, as measured by the bead surface-distance under gravity, correlates well with the probability of forming specific bonds. However, the unbinding rate was unaffected by the polymer.^[11] With improved precision, this method may provide a powerful tool for the study of adhesion dynamics at the single-molecule level.^[37]

6.2. Films and Model Membranes

6.2.1. Thin Films

Thin films of MgF₂ deposited on a glass cover-slide have been used for a long time to improve the contrast in RICM.^[9] RICM is particularly useful for studying wetting phenomena, on both uniform and patterned substrates.^[38] For example, the shape of a sessile droplet containing concentrated actin filaments has been characterized and the edge geometry has been related to the conformation and flow of the filaments^[39] (Figure 2B). Thin films of PDMS have also been characterized by RICM^[19] and used as a patterned substrate to monitor cell deformations in RICM.^[40,41]

6.2.2. Free Membrane Shapes

RICM has proved to be the method of choice to probe the configuration of model membranes that are bound to or hover near a substrate^[12,14,28,29,42,43] (also see refs. [44,45] and references therein for an overview). In one of the earliest applications, snapshots of the shape of a freely fluctuating membrane were reconstructed.^[8,28] This information was then used to deduce the dependence of the height on wavelength in the Fourier space, which in turn gave a convenient way to measure the bending elasticity of the fluctuating membrane using the theoretical model of Helfrich.^[44,46]

6.2.3. Contact Angle, Tension, Adhesion Energy and Vesicle Spreading Dynamics

A powerful application of RICM is to estimate the adhesion energy of a vesicle on a substrate. Like a liquid droplet, the equilibrium shape of an adhering vesicle is determined by a balance of forces which, for tightly adhering and relatively tense vesicles, yields the Young–Dupre law $W = \sigma(1 - \cos\theta)$, where W is the adhesion energy density, σ is the membrane tension and θ is the contact angle. It must be remembered that vesicles have a membrane that has a finite bending rigidity, which implies that the surface cannot support abrupt changes in slope, since that would involve prohibitively large membrane deformation energy. For this reason, the real microscopic contact angle must always be π ;^[47] however, a macro-

scopic contact angle can be defined and measured easily using RICM from reconstruction of the shape of the membrane in the radial direction. Under most circumstances,^[42,48] the tension σ too can be determined from the reconstructed shape via the so-called contact length λ . λ is defined as the distance from the point at which the membrane adheres to the substrate to the point at which the straight line representing the vesicle profile far from the substrate intersects the substrate. The shape of the membrane along the rim just outside the adhesion disc is determined by a balance of elastic deformation and membrane tension, which yields $\lambda = \sqrt{\kappa/\sigma}$.^[44] Thus, since θ and λ can be measured from the reconstructed height profile, and the bending rigidity κ is usually known for a given membrane composition, the adhesion energy density can be estimated.

With advances in the preparation of the mimetic GUV system, which can be made to be an increasingly realistic model of cells,^[12,14,29,42,49–52] RICM has been used to probe different aspects of adhesion. The evolution of the vesicle adhesion area with time has been measured.^[12,43,53] Recently, the evolution of the contact angle and the adhesion energy during the adhesion of a vesicle has been followed.^[53,54] Similarly, the evolution of the adhesion disc when the vesicle is submitted to an unbinding force has also been studied.^[15,13]

6.2.4. Topography of the Adhesion Disc

The procedure described in Section 5.5 enables the precise measurement of absolute membrane–substrate distance and, therefore, the construction of the precise topography of the adhesion disc. This in turn opens up the possibility of determining the binding configuration of large adhesion proteins, without crystallizing them and without the necessity of applying force as would be the case if techniques such as atomic force microscopy (AFM), micropipette aspiration (biomembrane-force probe, BFP) or surface force apparatus (SFA) were used.^[55,56] Furthermore, since membrane proteins are probed while they are membrane bound, the geometry mimics closely the real situation in a cell. This way of measuring protein dimensions was validated in a GUV/supported lipid bilayer (SLB) system using biotin/avidin-mediated binding as a model. The inter-membrane distance was found to be 7 ± 1 nm, which compares very well with the theoretical expectation of 8 nm.^[14] Subsequently, the technique was applied to adhesion mediated by E-cadherin (Ecad) extra-cellular moieties. Since Ecad has five extra-cellular domains, each capable of binding with an opposing partner, the precise configuration in which Ecad binds is a subject of ongoing debate. On the basis of force-induced unbinding experiments (see ref. [56], and references therein), three different binding configurations were proposed: overlap of only the outermost domains (EC01–EC01), of the three outermost domains (EC01–EC03–EC01–EC03) or of all five domains (EC01–EC05–EC01–EC05). In our force-free experiments, the inter-membrane distance was measured as 55 ± 10 nm, which implies that at least in the specific case of vesicle-to-bilayer adhesion, the Ecad binds predominantly in the (EC01–EC01) and the (EC01–EC03–EC01–EC03) configurations.^[14]

6.2.5. Dynamical RICM and Analysis of Thermal Fluctuations

It has already been demonstrated above how the thermal fluctuations of colloidal beads can be exploited to measure the local interaction potential and the friction. A similar quantitative analysis, called dynamical RICM (Dy-RICM) can be implemented for membranes. A pixel-by-pixel map of the membrane fluctuations is prepared by a frame-by-frame analysis of the height using either Equation (8) or Equation (9), and then calculation of the standard deviation of the membrane height from a temporal average. At the simplest level of analysis, the measured fluctuations are compared to the expected shot-noise to diagnose binding.^[12,13] Even at this crude level, complex and sub-optical features on the membrane become detectable^[13] and an underlying bond organization can be inferred.^[57] The technique was used to characterize a GUV/SLB system in which binding was mediated by RGD/integrin bonds.^[13] The integrins, present on the SLB, were either mobile or immobilized. In the latter case, Dy-RICM revealed bond clusters, invisible in RICM, which in addition could resist unbinding forces. In the mobile integrin case, adhesion domains formed from a dilute array of bonds, which were undetectable in RICM, showed up in a Dy-RICM analysis. These dilute bond clusters mature with time as well as under an external force into dense clusters detectable with RICM. Detection and understanding of the dilute bond clusters is crucial for a global understanding of the unusual behaviour of this system under an unbinding force, whereby adhesion domains are observed to grow passively upon force application.

A further improvement being implemented is the combination of dual-wave RICM and Dy-RICM.^[54,58] This allows for a refined quantification of the height measurements and thus opens up the way to the construction of the membrane–surface interaction potential.^[58] Further refinement of the Dy-RICM technique can be anticipated, where temporal information such as adhesion domain lifetimes will be probed.

6.3. Living Cells

6.3.1. Tight Adhesion

As detailed in Section 5.6, RICM (or more often IRM) has been used for a long time as a simple diagnostic of binding or static adhesion. Simultaneous RICM and fluorescence have repeatedly established that focal adhesions, as envisaged by marking, for example, vinculin, show up as dark patches in RICM.^[59–62] Recently, it has been shown that, contrary to expectations, such adhesion spots grow under a detaching force.^[59] In the case of non-focal adhesion forming cells, it was shown that dark adhesion patches represent tight adhesion to the extent that the cells exhibiting them do not detach under flow.^[63] In studies of immune cells too, RICM/IRM has been used to qualitatively diagnose binding topography which is then compared to data obtained with fluorescence labelling.^[64] A few studies have also addressed the contact between a neuronal growth cone and substrate coated with various proteins involved in adhesion or migration.^[65]

6.3.2. Adhesion Dynamics and Spreading

As fast recording and storing of wide-field images became technically possible, the interest in dynamical processes in cell biology, including cell spreading, grew.^[66,67] From about 2003 onwards, RICM has been extensively used to probe the dynamics of cell spreading^[30,31,63,68] together with theoretical modelling.^[69,70] Interestingly, in all these studies, the spreading of cells has been shown to follow a power law. Often, several stages of spreading—with different exponents for the power law—have been seen, both for cells that are habitually non-motile, such as fibroblasts,^[68,71] and for highly motile cells, such as neutrophils.^[30] In the case of the latter, it was shown that cell polarization, in terms of adhesion and spreading, occurs within seconds of activation and that the start of a directed motion of the cell coincides with the establishment of the first tight adhesion spot. RICM is arguably the most appropriate tool to study cell adhesion dynamics. A lot, however, remains to be done in terms of more quantitative analysis as well as imaging simultaneously with fluorescence.

6.3.3. Cell Membrane Fluctuations and Other Applications

Another interesting recent application concerns the dynamics of the cell membrane. Following procedures similar to those described in Section 5.5, it has been shown that the cell membrane undergoes fluctuations close to the substrate prior to adhesion.^[72,73] A relatively under-explored utilization is to follow exocytosis.^[74] In another innovative application, RICM was used to monitor simultaneously the regular patterned markings on a flexible substrate and the focal adhesion spots of cells adhering on it, to calculate the forces exerted by single-focal adhesions.^[40] Small features such as filopodia can be easily visualized in RICM but this capability has not been exploited much.

6.3.4. Using Dual-Wave RICM with Cells: Towards Better Quantification

An exciting domain of ongoing development is the application of dual-wave RICM to reconstruct cell membrane conformations. Here, we demonstrate qualitatively the proof of the principle on an adhering macrophage that forms a well-defined lamellipodium (Figure 13A). When illuminated with green light, the entire RICM image of the cell appears dark, whereas in blue light, the lamellipodium appears bright. The raw intensity along a radial line is plotted in Figure 13B and is normalized branch-by-branch (see Section 5.2.2) in Figure 13C. From inspection of Figure 13A, a naive interpretation would imply that the lamellipodium is detached from the surface and floats about 200 nm above the surface—such a scenario is shown in Figure 13D and the corresponding expected intensity profile is traced in Figure 13E. An alternative scenario is shown in Figure 13F (intensity profile: Figure 13G), where the lower surface is firmly attached to the slide but the upper surface of the lamellipodium reflects light that contributes to the interference pattern. Clearly, the real situation may be a mixture of these two

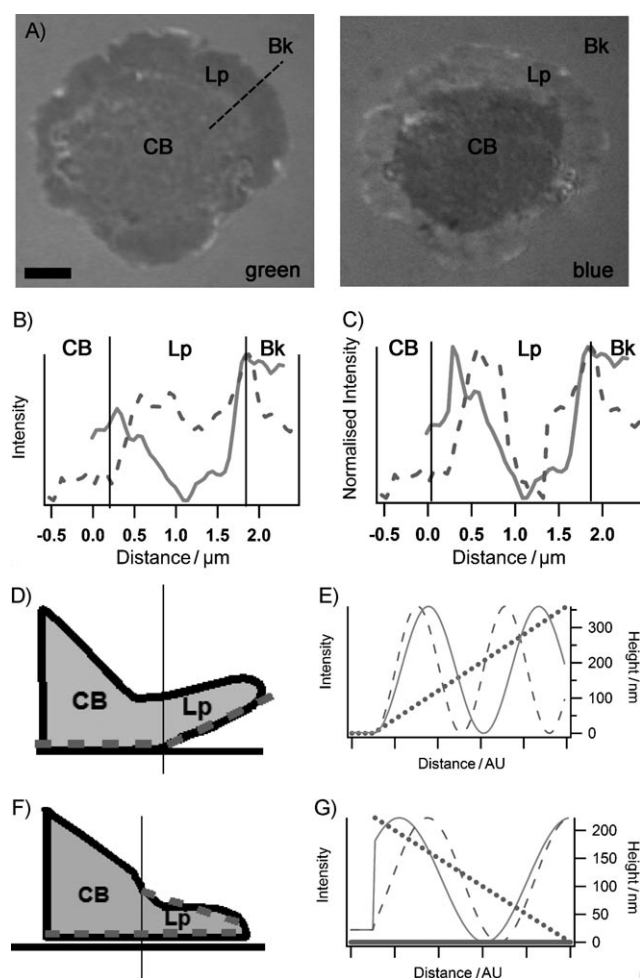


Figure 13. A) RICM of a macrophage (line J774) that is allowed to adhere to a glass slide functionalized with the protein invasins on which is grafted a layer of the extra-cellular matrix polymer hyaluronan, illuminated with green (546 nm) and blue (436 nm) light. CB: cell body, Lp: lamellipodium, Bk: background. Scale bar: 2 μm . B) Intensity in green (solid line) and blue (dashed line) channels in arbitrary units along the radial dashed line in (A). C) Blue and green intensities normalized branch-by-branch between 0 and 1. D, F) Two possible scenarios for the configuration of the lamellipodium. The dotted line indicates the simplified profile that is assumed for calculations. E, G) The corresponding expected normalized intensities (—: green; - - - -: blue) for the assumed height profile (.....).

extreme scenarios but we shall consider, for simplicity, only the two simplest cases. A qualitative inspection of the experimental curve, tracing it from right to left, reveals the following sequence. First, the substrate is encountered, then a peak in both blue and green intensity at the edge of the lamellipodium. Next, the blue intensity drops and reaches a minimum and begins to climb again. The green intensity also drops but reaches its minimum after the blue. Finally, the intensity climbs for both the wavelengths and first the blue and then the green reach their respective maximum and begin to drop off. A comparison with the intensity curve presented in Figure 13E shows that going from right to left, there is no height for which the blue channel reaches its minimum before the green. However, comparison with Figure 13G shows that if the thick-

ness of the lamellipodium begins to increase from roughly zero, the theoretical profile qualitatively accounts for all the features seen in the experimental curve. Thus, we conclude that the lamellipodium is in fact firmly attached to the substrate.

In the above explanation, we have demonstrated qualitatively the use of dual-wave RICM to choose between two different simple scenarios. Similar ideas can serve as the basis of quantitative reconstruction of the entire shape of the lamellipodium, but require more involved numerical calculations as well as use of either a third wavelength or difference illumination angles to supplement the available information.

7. Outlook

We have presented some recent developments in the technique of RICM and have illustrated new applications in soft matter and cell adhesion. The power of RICM lies in its easy implementation, the absence of requirements for labelling or staining the sample, the access to fast (10 ms) dynamic processes, and the possibility of combining it with other microscopic techniques or micro-manipulations. Its drawback is mainly in the complexity of image interpretation, especially for quantitative analyses. This issue arises from the fact that in RICM, optical paths (a product of geometrical length and refractive index), rather than absolute distances, are measured. We indicate below the possible directions for future developments that could overcome the above issue.

The combination of RICM with other surface microscopies appears to be a promising avenue. For example, combination with total internal reflection fluorescence (TIRF) microscopy should 1) permit a cross-validation of current models for membrane shape reconstruction and 2) offer a combined time-lapse monitoring of the membrane and specific proteins on the membrane or the cytoskeleton during dynamic cell processes. The RICM signal can also be enhanced by using anti-reflecting substrates offering a good reproducibility in optical properties together with compatibility with the chemistry of glass functionalization. An important challenge would be to use the spectral variation of refractive index to determine length independently of material optical properties.

A theoretical effort is also required to fully combine the information obtained at multiple wavelengths and automatize the reconstruction of complex membrane conformations. While simple algorithms may be sufficient for quasi-flat membranes imaged at low INA, more powerful methods of optics such as ray tracing may be required to analyse images of convoluted membranes obtained with high INA.

Finally, RICM has to demonstrate its performance on non-flat substrates, which are increasingly used to probe the micro and nano properties of cell functions.^[75] With the recent discoveries concerning the interaction of light with sub-optical features, exciting perspectives arise for the development of RICM on nanostructured substrates.

Acknowledgements

We thank A. Zidowska and E. Sackmann for the experiment described in Figure 13.

Keywords: cell adhesion • colloids • membranes • reflection interference contrast microscopy • soft matter

- [1] A. S. Curtis, *J. Cell Biol.* **1964**, *20*, 199–215.
- [2] J. S. Ploem, *Reflection–Contrast Microscopy as a Tool for Investigation of the Attachment of Living Cells to a Glass Surface*, Blackwell, Oxford, **1975**.
- [3] J. Bereiter-Hahn, C. H. Fox, B. Thorell, *J. Cell Biol.* **1979**, *82*, 767–779.
- [4] B. Geiger, Z. Avnur, T. E. Kreis, J. Schlessinger, *Cell Muscle Motil.* **1984**, *5*, 195–234.
- [5] H. Verschuere, *J. Cell Sci.* **1985**, *75*, 279–301.
- [6] I. Weber, *Methods Enzymol.* **2003**, *361*, 34–46.
- [7] T. J. Filler, E. T. Peuker, *J. Pathol.* **2000**, *190*, 635–638.
- [8] A. Zilker, H. Engelhard, E. Sackmann, *J. Phys. France* **1987**, *48*, 2139–2151.
- [9] J. O. Rädler, E. Sackmann, *J. Phys. II* **1993**, *3*, 727–748.
- [10] J. Schilling, K. Sengupta, S. Goennenwein, A. R. Bausch, E. Sackmann, *Phys. Rev. E* **2004**, *69*, 021901.
- [11] P. Robert, K. Sengupta, P.-H. Puech, P. Bongrand, L. Limozin, *Biophys. J.* **2008**, *95*, 3999–4012.
- [12] L. Limozin, K. Sengupta, *Biophys. J.* **2007**, *93*, 3300–3313.
- [13] A.-S. Smith, K. Sengupta, S. Goennenwein, U. Seifert, E. Sackmann, *Proc. Natl. Acad. Sci. USA* **2008**, *105*, 6906–6911.
- [14] S. F. Fenz, R. Merkel, K. Sengupta, *Langmuir* **2009**, *25*, 1074–1085.
- [15] A.-S. Smith, B. G. Lorz, S. Goennenwein, E. Sackmann, *Biophys. J.* **2006**, *90*, L52–L54.
- [16] V. Heinrich, W. P. Wong, K. Halvorsen, E. Evans, *Langmuir* **2008**, *24*, 1194–1203.
- [17] M. Born, E. Wolf, *Principles of Optics, 7th ed.*, Cambridge University Press, Cambridge; UK, **1999**.
- [18] M. Pluta, *Advanced Light Microscopy*, Elsevier, Amsterdam, **1998**.
- [19] K. Prechtel, *Wetting and Interdiffusion: Establishment of a Biocompatible System and Measurements of its Dynamics*, PhD thesis, Technical University Munich, **2005**.
- [20] D. Gingell, I. Todd, *Biophys. J.* **1979**, *26*, 507–526.
- [21] M. Kühner, E. Sackmann, *Langmuir* **1996**, *12*, 4866–4876.
- [22] G. Wiegand, K. R. Neumaier, E. Sackmann, *J. Appl. Opt.* **1998**, *37*, 6892–6905.
- [23] K. Sengupta, J. Schilling, S. Marx, M. Fischer, A. Bacher, E. Sackmann, *Langmuir* **2003**, *19*, 1775–1781.
- [24] C. Picart, K. Sengupta, J. Schilling, G. Maurstad, G. Ladam, A. Bausch, E. Sackmann, *J. Phys. Chem. B* **2004**, *108*, 7196–7205.
- [25] R. P. Richter, K. K. Hock, J. Burkhartsmeyer, H. Boehm, P. Bingen, G. Wang, N. F. Steinmetz, D. J. Evans, J. P. Spatz, *J. Am. Chem. Soc.* **2007**, *129*, 5306–5307.
- [26] K. Kim, O. A. Saleh, *Appl. Opt.* **2008**, *47*, 2070–2075.
- [27] S. Fenz, *Cell–Cell Adhesion Mediated by Mobile Ligand–Receptor Pairs: A Biomimetic Study*, PhD thesis, Forschung Zentrum Juelich, **2009**.
- [28] J. O. Rädler, T. J. Feder, H. H. Strey, E. Sackmann, *Phys. Rev. E* **1995**, *51*, 4526–4536.
- [29] S. Marx, J. Schilling, E. Sackmann, R. Bruinsma, *Phys. Rev. Lett.* **2002**, *88*, 138102.
- [30] K. Sengupta, H. Aranda-Espinoza, L. Smith, P. Janmey, D. Hammer, *Biophys. J.* **2006**, *91*, 4638–4648.
- [31] A. Hategan, K. Sengupta, S. Kahn, E. Sackmann, D. E. Discher, *Biophys. J.* **2004**, *87*, 3547–3560.
- [32] N. G. Clack, J. T. Groves, *Langmuir* **2005**, *21*, 6430–6435.
- [33] J. C. Crocker, D. G. Grier, *Phys. Rev. Lett.* **1994**, *73*, 352–355.
- [34] J. O. Rädler, E. Sackmann, *Langmuir* **1992**, *8*, 848–853.
- [35] A. Albersdörfer, E. Sackmann, *Eur. Phys. J. B* **1999**, *10*, 663–672.
- [36] G. Maurstad, A. R. Bausch, P. Sikorski, B. T. Stokke, *Macromol. Symp.* **2005**, *227*, 161–172.
- [37] P. Robert, *Étude Dynamique de l'Adhésion Leucocytaire avec une Chambre à Flux Laminaire: de la Physique à la Médecine*, PhD thesis, Aix-Marseille Université, **2009**.
- [38] G. Wiegand, T. Jaworek, G. Wegner, E. Sackmann, *J. Colloid Interface Sci.* **1997**, *196*, 299–312.
- [39] L. Vonna, L. Limozin, A. Roth, E. Sackmann, *Langmuir* **2005**, *21*, 9635–9643.
- [40] R. Merkel, N. Kirchgessner, C. M. Cesa, B. Hoffmann, *Biophys. J.* **2007**, *93*, 3314–3323.
- [41] C. M. Cesa, N. Kirchgessner, D. Mayer, U. S. Schwarz, B. Hoffmann, R. Merkel, *Rev. Sci. Instrum.* **2007**, *78*, 034301.
- [42] A. Albersdörfer, T. Feder, E. Sackmann, *Biophys. J.* **1997**, *73*, 245–257.
- [43] A. Boulbitch, Z. Guttenberg, E. Sackmann, *Biophys. J.* **2001**, *81*, 2743–2751.
- [44] E. Sackmann, R. F. Bruinsma, *ChemPhysChem* **2002**, *3*, 262–269.
- [45] A.-S. Smith, E. Sackmann, *ChemPhysChem* **2009**, *10*, 66–78.
- [46] W. Helfrich, *Z. Naturforsch.* **1973**, *28*, 693–703.
- [47] U. Seifert, R. Lipowsky, *Phys. Rev. A* **1990**, *42*, 4768–4771.
- [48] *Adhesion and Rolling of Leukocytes: A Physical Model*, R. Bruinsma in *Physics of Biomaterials, NATO Science Series, ASI*, Geilo, **1995**.
- [49] A. Kloboucek, A. Behrisch, J. Faix, E. Sackmann, *Biophys. J.* **1999**, *77*, 2311–2328.
- [50] S. Goennenwein, M. Tanaka, B. Hu, L. Moroder, E. Sackmann, *Biophys. J.* **2003**, *85*, 646–655.
- [51] L. Limozin, A. Roth, E. Sackmann, *Phys. Rev. Lett.* **2005**, *95*, 178101.
- [52] B. G. Lorz, A.-S. Smith, C. Gege, E. Sackmann, *Langmuir* **2007**, *23*, 12293–12300.
- [53] D. Cuvelier, P. Nassoy, *Phys. Rev. Lett.* **2004**, *93*, 228101.
- [54] K. Sengupta, L. Limozin, *unpublished results*.
- [55] K. C. Neuman, A. Nagy, *Nat. Methods* **2008**, *5*, 491–505.
- [56] D. Leckband, A. Prakasam, *Annu. Rev. Biomed. Eng.* **2006**, *8*, 259–287.
- [57] A. Smith, S. F. Fenz, K. Sengupta, *unpublished results*.
- [58] C. Monzel, S. F. Fenz, R. Merkel, K. Sengupta, *ChemPhysChem*, **2009**, *10*, 2828–2838.
- [59] D. Riveline, E. Zamir, N. Q. Balaban, U. S. Schwarz, T. Ishizaki, S. Narumiya, Z. Kam, B. Geiger, A. D. Bershadsky, *J. Cell Biol.* **2001**, *153*, 1175–1186.
- [60] J. Lee, K. Jacobson, *J. Cell Sci.* **1997**, *110*, 2833–2844.
- [61] R. M. Saunders, M. R. Holt, L. Jennings, D. H. Sutton, I. L. Barsukov, A. Bobkov, R. C. Liddington, E. A. Adamson, G. A. Dunn, D. R. Critchley, *Eur. J. Cell Biol.* **2006**, *85*, 487–500.
- [62] M. R. Holt, Y. Calle, D. H. Sutton, D. R. Critchley, G. E. Jones, G. A. Dunn, *J. Microsc.* **2008**, *232*, 73–81.
- [63] A. Pierres, P. Eymeric, E. Baloche, D. Touchard, A.-M. Benoliel, P. Bongrand, *Biophys. J.* **2003**, *84*, 2058–2070.
- [64] S. C. Bunnell, V. A. Barr, C. L. Fuller, L. E. Samelson, *Sci. STKE* **2003**, *2003*, PL8.
- [65] J. Drazba, P. Liljelund, C. Smith, R. Payne, V. Lemmon, *Brain Res. Dev. Brain Res.* **1997**, *100*, 183–197.
- [66] B. J. Dubin-Thaler, G. Giannone, H.-G. Döbereiner, M. P. Sheetz, *Biophys. J.* **2004**, *86*, 1794–1806.
- [67] C. A. Reinhart-King, M. Dembo, D. A. Hammer, *Biophys. J.* **2005**, *89*, 676–689.
- [68] D. Cuvelier, M. Théry, Y.-S. Chu, S. Dufour, J.-P. Thiéry, M. Bornens, P. Nassoy, L. Mahadevan, *Curr. Biol.* **2007**, *17*, 694–699.
- [69] T. Frisch, O. Thoumine, *J. Biomech.* **2002**, *35*, 1137–1141.
- [70] F. Chamaroux, S. Fache, F. Bruckert, B. Fourcade, *Phys. Rev. Lett.* **2005**, *94*, 158102.
- [71] H.-G. Döbereiner, B. Dubin-Thaler, G. Giannone, H. S. Xenias, M. P. Sheetz, *Phys. Rev. Lett.* **2004**, *93*, 108105.
- [72] A. Zidowska, E. Sackmann, *Phys. Rev. Lett.* **2006**, *96*, 048103.
- [73] A. Pierres, A.-M. Benoliel, D. Touchard, P. Bongrand, *Biophys. J.* **2008**, *94*, 4114–4122.
- [74] A. Llobet, V. Beaumont, L. Lagnado, *Neuron* **2003**, *40*, 1075–1086.
- [75] K. Sengupta, E. Moyen, M. Mace, A.-M. Benoliel, A. Pierres, F. Thibaudau, L. Masson, L. Limozin, P. Bongrand, M. Hanbucken, *Small* **2009**, *5*, 449–453.

Received: July 29, 2009

Published online on October 8, 2009